Review Article

Liheng Bian, Jinli Suo*, Qionghai Dai and Feng Chen

Fourier ptychography for high space-bandwidth product microscopy

https://doi.org/10.1515/aot-2017-0054
Received August 30, 2017; accepted October 8, 2017

Abstract: Fourier ptychography is a novel imaging technique with high space-bandwidth product (SBP) on the scale of gigapixel, and has been successfully applied for high-resolution and large field-of-view (FOV) microscopy, termed Fourier ptychographic microscopy (FPM). FPM utilizes a low-numerical-aperture objective lens to capture multiple large FOV but low-resolution images under angularly varying illumination, and uses phase-retrieval algorithms to reconstruct the sample's high-resolution amplitude and phase information. FPM is advantageous over conventional high SBP microscopy techniques in many aspects, including no mechanical scanning, computational acquisition of both amplitude and phase, extended depth of focus, long working distance, and high compatibility with current microscopes. In this paper, we review FPM with its principles, multiple techniques to improve its performance, and its various applications and extensions.

Keywords: aperture synthesis; Fourier ptychography; high space-bandwidth product; microscopy; phase retrieval.

1 Introduction

In microscopy, both high resolution (HR) and large field of view (FOV) are desirable for various biomedical applications such as digital pathology, hematology, immunohistochemistry, and neuroanatomy [1]. However, there is a tradeoff between these two goals due to the limited information throughput of imaging systems, which is usually characterized by space-bandwidth product (SBP). SBP is defined as $\frac{\text{image area}}{(0.5\times\text{resolution})^2}$ standing for the total number of resolvable pixels of an imaging system [2]. The 0.5 factor comes from the Nyquist sampling theorem [3]. SBPs of most off-the-shelf objective lenses are usually in megapixels, regardless of their magnification factors and numerical apertures (NA). For example, a standard 2× microscope objective lens (Plan APO, 0.08 NA, Olympus) has a resolution of 4 μm and an FOV of 120 mm^2, corresponding to an SBP of ~30 megapixels. Similarly, a standard 20× microscope objective lens (PLN 20×, 0.4 NA, Olympus) owns a resolution of 0.8 μm and an FOV with a 1.1-mm diameter, corresponding to an SBP of ~8 megapixels. To sum up, there is always a tradeoff between achievable resolution and FOV of imaging systems.

To increase the information throughput of a microscope, the most intuitive idea is to scale up the size of the objective lens to enlarge FOV and improve resolution. However, the geometrical aberrations of the lens also scale up as its size increases. As a result, more lenses are needed to compensate the aberrations. The resulting lens system is expensive to produce and difficult to align and, thus, impractical for a high SBP microscope. Another way for large information throughput is introducing sample scanning to enlarge FOV under the premise of high resolution, such as the whole slide imaging (WSI) technique [4]. However, the introduced mechanical scanning requires precise control, which largely increases the system's complexity.

Fourier ptychography (FP) is a recently proposed technique for high SBP imaging [1, 5]. Different from WSI, FP sequentially captures a set of low-resolution (LR) images but with large FOV, which describe different spatial-frequency sub-spectra of the scene in Fourier space [6]. Then it stitches these images together in Fourier space to reconstruct the entire spatial-frequency spectrum and HR image of the target scene. FP has been successfully applied to high SBP microscopy, termed Fourier ptychographic microscopy (FPM) [1, 7]. FPM simply replaces the conventional illumination source of a microscope with a light-emitting-diode (LED) array to provide angularly varying illumination, and utilizes a low-NA objective lens to capture multiple LR images. Utilizing phase-retrieval algorithms [8–10], FPM is able to reconstruct both the

***Corresponding author: Jinli Suo,** Department of Automation, Tsinghua University, Beijing 100084, China, e-mail: jlsuo@tsinghua.edu.cn
Liheng Bian, Qionghai Dai and Feng Chen: Department of Automation, Tsinghua University, Beijing 100084, China

www.degruyter.com/aot

sample's HR amplitude and phase by stitching the captured LR images together in Fourier space. As stated in Ref. [1], the synthetic NA of the reported FPM prototype setup reaches ~0.5, and the FOV is ~120 mm^2 that keeps the same with the utilized 2× objective lens. Using a 40× 0.75-NA objective lens, the FPM setup reported in Ref. [11] has a synthetic NA of 1.45, which is usually only achievable by using oil immersion objectives. Besides increasing the NA of the objective lens, Sun et al. [12] utilized an oil immersion condenser to increase the illumination NA to 1.2. To conclude, the FPM technique greatly increases the information throughput of existing microscopes. Besides, utilizing a computational wavefront correction strategy [1], FPM can achieve a resolution-invariant depth of focus of ~0.3 mm. In contrast, the depth of focus of a standard 2× objective lens (Plan APO, 0.08 NA, Olympus) is ~80 μm.

FPM is advantageous over conventional high SBP microscopy techniques in multiple aspects. First, FPM is free of mechanical scanning. It simply turns different LEDs on and capture the corresponding images. Second, there is no interferometric detection module for phase measuring. Instead, the phase information is reconstructed by phase-retrieval algorithms from the intensity measurements [5]. Third, the computational imaging scheme allows to expand the depth of focus beyond the conventional optical limits. Fourth, FPM has a longer working distance than other high-NA microscopes due to the utilized low-NA objective lens. Fifth, FPM has high compatibility with existing microscopes because it only needs to replace the illumination source with an LED array. Because of its simple configuration and superior performance, FPM owns great potentials for various biological applications and has been demonstrated for tumor cell enumeration and analysis [13], digital pathology [14], blood cell counting [15], and cell culture imaging [16].

As FPM was proposed, there have been a number of studies concerning its performance improvement and extensions. In this article, we review FPM with its principles, multiple techniques improving its performance (shortening capture time, increasing robustness to measurement noise, and correcting system aberrations), and its various extensions. We hope this helps to promote a comprehensive understanding of FPM and its further commercialization and applications.

2 Principles of FPM

An exemplar FPM setup is shown in Figure 1A. It simply replaces the illumination source of a commercial microscope with an LED array to provide angularly varying illumination. In the next, we begin to introduce the image formation and reconstruction of FPM.

2.1 Image formation

FPM is a coherent imaging technique [7]. It requires the illumination to be coherent [1], or partially coherent [7, 17], to ensure the correlation between the change of illumination angle and the spatial-frequency spectrum shift in Fourier space [6]. Under the assumption that the light incident on a sample is a plane wave, the optical field transmitted from the sample can be described as $\phi(x, y)e^{\left(jx\frac{2\pi}{\lambda}\sin\theta_x, jy\frac{2\pi}{\lambda}\sin\theta_y\right)}$, where ϕ is the sample's complex spatial map, (x, y) are the two-dimensional (2D) spatial coordinates, j is the imaginary unit, λ is the wavelength of illumination, and (θ_x, θ_y) are the incident angles as shown in Figure 1B. The optical field is then Fourier transformed to the pupil plane when it travels through the objective lens and, subsequently, low-pass filtered by the aperture. This process can be denoted as $P(k_x, k_y)\mathcal{F}(\phi(x, y)e^{\left(jx\frac{2\pi}{\lambda}\sin\theta_x, jy\frac{2\pi}{\lambda}\sin\theta_y\right)})$, where $P(k_x, k_y)$ is the pupil function (the coherent transfer function of the objective lens), (k_x, k_y) are the 2D spatial-frequency coordinates in the pupil plane, and $\mathcal{F}$ is the Fourier transform operator. Afterward, the optical field is Fourier transformed again when it passes through the tube lens to the imaging sensor. Because real imaging sensors can only capture light's intensity, the image formation of FPM follows

$$\begin{aligned}\mathbf{I} &= \left|\mathcal{F}^{-1}\left[P(k_x, k_y)\,\mathcal{F}(\phi(x, y)e^{\left(jx\frac{2\pi}{\lambda}\sin\theta_x, jy\frac{2\pi}{\lambda}\sin\theta_y\right)})\right]\right|^2 \\ &= \left|\mathcal{F}^{-1}\left[P(k_x, k_y)\Phi\left(k_x - \frac{2\pi}{\lambda}\sin\theta_x, k_y - \frac{2\pi}{\lambda}\sin\theta_y\right)\right]\right|^2, \end{aligned} \quad (1)$$

where $\mathbf{I}$ is the captured image, $\mathcal{F}^{-1}$ is the inverse Fourier transform operator, and Φ is the spatial-frequency spectrum of the sample. From Eq. (1), we can see that different illumination angles $\{\theta_x, \theta_y\}$ result in different shifts $\left\{\frac{2\pi}{\lambda}\sin\theta_x, \frac{2\pi}{\lambda}\sin\theta_y\right\}$ of the sample's HR spatial-frequency spectrum in Fourier space. By sequentially turning on the LEDs at different positions, we capture multiple LR images describing different spatial-frequency sub-spectra of the sample. Visual explanation of the image formation process is diagrammed in Figure 1B.

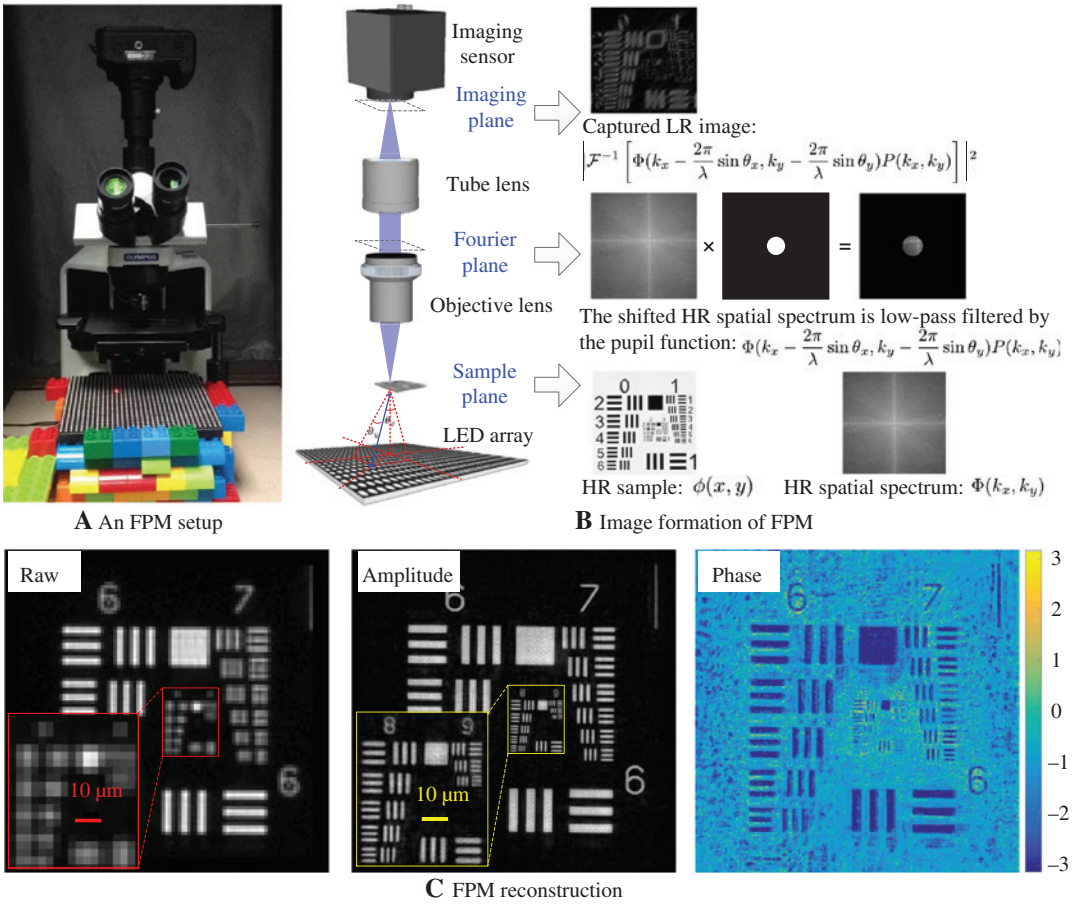

Figure 1: The FPM system. (A) An FPM setup. (B) Image formation of FPM. (C) FPM reconstruction.

Because the Fourier transform ($\mathcal{F}$ and $\mathcal{F}^{-1}$) is linear, and $P(k_x, k_y)\Phi\left(k_x-\frac{2\pi}{\lambda}\sin\theta_x, k_y-\frac{2\pi}{\lambda}\sin\theta_y\right)$ is a linear operation that passes only a finite bandwidth of the sample's spatial-frequency spectrum, we can rewrite the above image formation as

$$\mathbf{b}=|\mathbf{Az}|^2, \tag{2}$$

where $\mathbf{b}\in\mathbb{R}^m$ stands for the intensity measurements (all the captured images $\mathbf{I}$ aligned in a vector), $\mathbf{A}\in\mathbb{C}^{m\times n}$ is the linear transform matrix incorporating both the Fourier transform and the low-pass filtering, and $\mathbf{z}\in\mathbb{C}^n$ is the sample's HR spatial spectrum (Φ in vector form).

2.2 FPM reconstruction

As formulated in Eq. (2), the FPM reconstruction could be treated as a typical phase-retrieval process, which aims to recover a complex function given its linearly transformed intensity measurements. Specifically, we only obtain the intensity images corresponding to different sub-bands of the sample's HR spatial-frequency spectrum and intend to retrieve the complex HR spectrum.

Conventional FPM [1, 5] utilizes the alternating projection (AP) algorithm [8, 9], a widely used iterative method for phase retrieval, to implement the reconstruction. The AP algorithm switches between the Fourier and spatial domains, and add respective support constraints to perform optimization. In the FPM reconstruction, corresponding supports include the captured LR images used in the spatial domain, and the pupil function used in the Fourier domain. Mathematically, the reconstruction starts with an initialization of the HR image as $\phi_h=\sqrt{\mathbf{I}_h}$, where $\mathbf{I}_h$ is the upsampled version of the LR image captured under normal illumination, and the subscript h stands for high resolution. The Fourier transform of ϕ_h creates the initialization of the HR spatial-frequency spectrum $\Phi_h=\mathcal{F}(\phi_h)$. Then, the iteration begins for variable update. In each iteration, we successively utilize each captured image $\mathbf{I}$ to update Φ_h. Specifically,

by denoting the LR optical field at the detector as $\phi_l = \mathcal{F}^{-1}\left[P(k_x, k_y)\Phi_h\left(k_x - \frac{2\pi}{\lambda}\sin\theta_x, k_y - \frac{2\pi}{\lambda}\sin\theta_y\right)\right]$, where the subscript l stands for low resolution, we first use $\sqrt{\mathbf{I}}$ to replace ϕ_l's amplitude as

$$\phi_l' = \sqrt{\mathbf{I}}\frac{\phi_l}{|\phi_l|}. \tag{3}$$

Its Fourier transform $\Phi_l' = \mathcal{F}(\phi_l')$ is then utilized to update the corresponding sub-band of the sample's HR spatial-frequency spectrum as [18]

$$\begin{aligned}\Phi_h' = \Phi_h + \\ \frac{P^*\left(k_x - \frac{2\pi}{\lambda}\sin\theta_x, k_y - \frac{2\pi}{\lambda}\sin\theta_y\right)}{\left|P^*\left(k_x - \frac{2\pi}{\lambda}\sin\theta_x, k_y - \frac{2\pi}{\lambda}\sin\theta_y\right)\right|^2_{\max}} \\ \left[\Phi_l'\left(k_x - \frac{2\pi}{\lambda}\sin\theta_x, k_y - \frac{2\pi}{\lambda}\sin\theta_y\right)\right. \\ \left. -\Phi_l\left(k_x - \frac{2\pi}{\lambda}\sin\theta_x, k_y - \frac{2\pi}{\lambda}\sin\theta_y\right)\right].\end{aligned} \tag{4}$$

Following the above update principles, each captured image is utilized to update Φ_h in the iteration, and we repeat the iteration multiple times until convergence. The converged solution Φ_h is transformed back to the spatial domain to produce the sample's HR optical field ϕ_h with an increased SBP (high resolution and wide FOV).

When the sample is out of focus [1], an additional defocus phase factor $e^{i\frac{2\pi}{\lambda}\sqrt{1-(\sin\theta_x)^2-(\sin\theta_y)^2}z_0}$ is correspondingly added to the pupil function, where z_0 is the defocus distance. Correspondingly, the LR target optical field at the detector becomes

$$\phi_l = \mathcal{F}^{-1}\left[P(k_x, k_y)\Phi_h\left(k_x - \frac{2\pi}{\lambda}\sin\theta_x, k_y - \frac{2\pi}{\lambda}\sin\theta_y\right)\right. \\ \left. e^{i\frac{2\pi}{\lambda}\sqrt{1-(\sin\theta_x)^2-(\sin\theta_y)^2}z_0}\right].$$

When updating the HR spatial-frequency spectrum, we need to compensate the defocus phase as $\Phi_l' = \mathcal{F}(\phi_l')e^{-i\frac{2\pi}{\lambda}\sqrt{1-(\sin\theta_x)^2-(\sin\theta_y)^2}z_0}$ for successive updating as Eq. (4). Following this computational wavefront correction strategy, the depth of focus of FPM can be significantly extended beyond that of the utilized objective lens.

2.3 FPM requirements

For an FPM system to work successfully, the following requirements need to be satisfied. (I) Enough overlap between adjacent spatial-frequency sub-spectra is required to ensure the convergence of reconstruction. This correspondingly determines that the incident angle difference between adjacent LEDs should not be too big. As studied in Ref. [19], the reconstruction quality degrades as the sub-spectrum overlap ratio decreases, and a minimum of ~35% overlap ratio is needed for successful FPM reconstruction. This redundancy is necessary because both amplitude and phase information need to be recovered from the intensity measurements, and it is determined by the information theory that measurements should be more than signals to be reconstructed [8, 9, 20, 21]. For example, a recently proposed phase-retrieval algorithm termed Wirtinger flow algorithm [22, 23] needs at least 6 times measurements of signals for successful reconstruction. Assuming that the ratio between the overlapped sub-spectrum and the entire sub-spectrum is r, and we capture $n\times n$ LR images each with $m\times m$ pixels, then, the number of signals to be reconstructed including both amplitude and phase is $2\times[(1-r)m(n-1)+m]^2$, and the corresponding sampling ratio between measurements and signals is

$$\eta = \frac{m^2n^2}{2\times\left[(1-r)m(n-1)+m\right]^2} \approx \frac{1}{2(1-r)^2}.$$

(II) The Nyquist sampling theory requires that the pixel size of the captured raw images should be no larger than $\frac{\lambda}{2\mathrm{NA}_{\mathrm{obj}}}$, where $\mathrm{NA}_{\mathrm{obj}}$ denotes the numerical aperture of the utilized objective lens. This ensures that we can theoretically achieve the resolution limit of the objective lens without a pixel aliasing problem [24].

3 Improvements of FPM

Although FPM is a powerful technique for high SBP imaging, there is a lot of room improving its performance for wider applications. In the next, we present multiple techniques that have been proposed to improve FPM.

3.1 Shortening capture time

Because FPM captures multiple images to increase SBP, its frame rate is relatively low. For example, it takes the FPM

setup reported in Ref. [1] ~3 min to capture the total 137 LR images for reconstructing one HR image. However, many biomedical applications such as neuroscience require dynamic imaging. Therefore, the capture time of FPM needs to be shortened.

An intuitive idea is to reduce shot number (the number of captured images). Bian et al. [25] studied the sparsity statistic of the natural images' spatial-frequency spectra in Fourier space and proposed a content adaptive illumination strategy, which allows FPM to capture only the most informative parts of the scene's spatial-frequency spectrum. As shown in Figure 2A, the capture order of the method is from low spatial frequencies to high spatial frequencies, which is different from the conventional FPM. When the amplitude of sub-spectrum is small, the corresponding LR image is not captured. Experiments show that the technique can save around 30–60% capture of the conventional FPM. Different from the adaptive capture strategy, Zhang et al. [29] used the LR image captured under normal illumination to determine all the

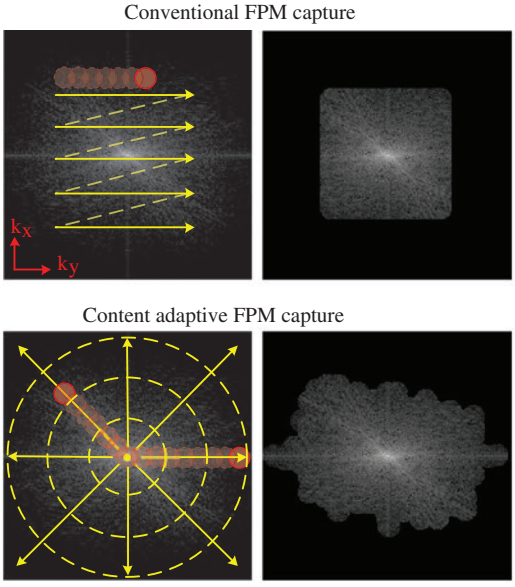

A Selectively capture in FPM [25]

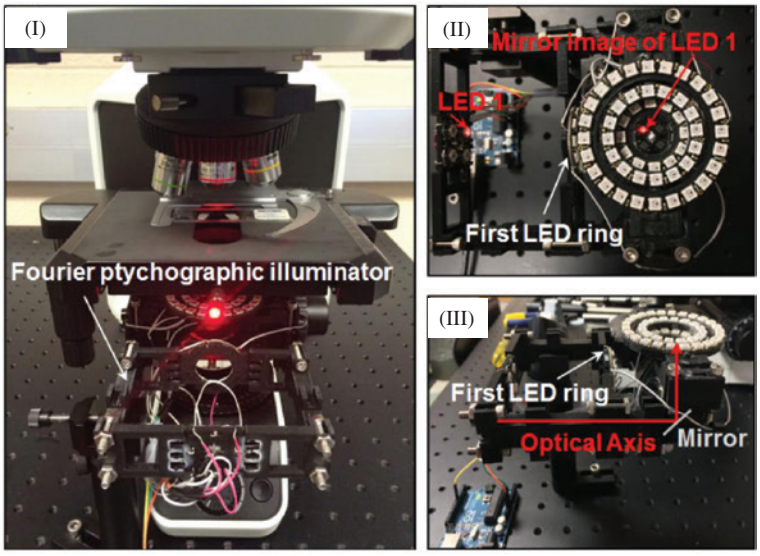

B The dome illuminator in ref. [26]

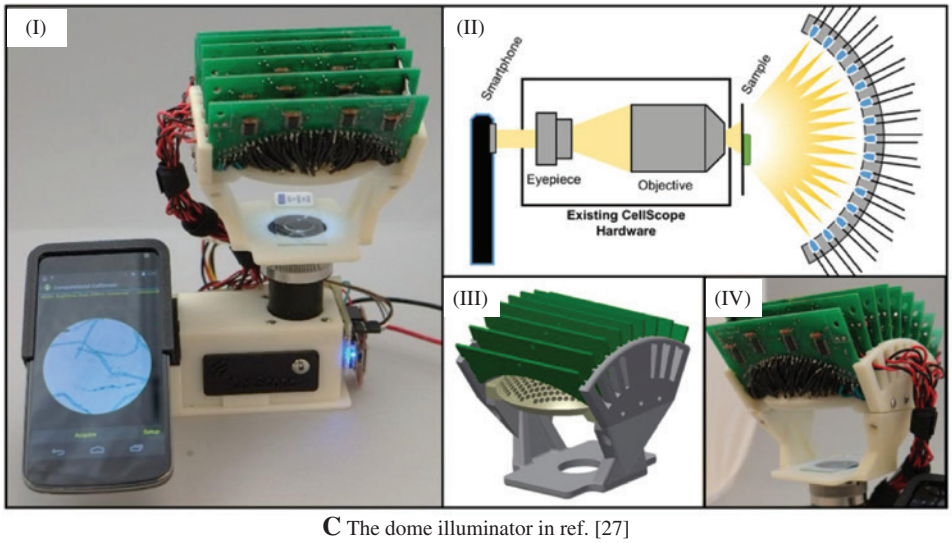

C The dome illuminator in ref. [27]

D The laser FPM [28]

Figure 2: Illumination optimization for faster FPM capture. (A) The comparison of capture strategy between the conventional FPM and the adaptive Fourier ptychography technique proposed in Ref. [25]. (B) and (C) Two developed dome illuminators [26, 27] are shown, respectively. (D) The laser FPM setup reported in Ref. [28].

sub-spectra that need to be captured at one time. This method owns less computation but lower accuracy. Dome-shaped illuminators are also developed by mounting LEDs onto a 3D-printed plastic case, as shown in Figure 2B and C. They own the ability to reduce the shot number by at least 50% benefiting from the round sampling strategy (LEDs are turned on in a round manner) [26, 27]. Besides, as the LEDs are distributed in a dome shape and oriented directly at the sample, the illuminators own higher illumination efficiency and, thus, further help reduce exposure time.

Another way to reduce capture time is to decrease exposure time. As stated in Ref. [1], the conventional FPM setup needs to capture three images under different exposure time for each LED, in order to obtain a high dynamic-range image free of overexposed or underexposed pixels. However, as studied in Ref. [19], one can selectively use partial pixels to obtain comparable reconstruction quality. In other words, the overexposed and underexposed regions can be kept unchanged, while the other regions are updated using corresponding intensity measurements. Using this method, one is able to bypass the HDR capture and combination process of the original FPM platform and shorten acquisition time by ~50%.

One can also increase illumination power to reduce exposure time. Ref. [30] demonstrated that using a high-power laser beam coupled with a digital micromirror device (DMD) can overcome the power limitation of LEDs. However, the illumination efficiency is low because only a small portion of the entire laser beam is utilized for each incident angle. To take full advantage of the laser's strong power, Chung et al. [28] utilized a mirror array and a 2D scanning Galvo mirror system to provide plane-wave illumination with diverse incidence angles, as shown in Figure 2D. In their prototype, a 1-W laser is applied to provide a collimated beam with the power of 150 mW and the beam diameter of 1 cm, allowing for the total capture time of 0.96 s.

Multiplexing is another method widely used to reduce both shot number and exposure time. Based on this technique, Tian et al. [31] proposed to turn on multiple LEDs at the same time for each capture, which is different from the conventional FPM strategy that sequentially turns on each single LED. The method achieves similar results with approximately an order of magnitude reduction in capture time. Later, they extended the technique to *in vitro* imaging by optimizing the multiplexing code, utilizing real-time hardware control, and developing an algorithm with a new initialization scheme [32]. Different from the above scheme that multiplexes illumination of the same wavelength, Dong et al. [17] multiplexed illumination of different colors to accelerate color imaging, and Zhou et al. [33] multiplexed color illumination to simultaneously acquire different spatial-frequency sub-spectra for fast monochromatic imaging.

3.2 Increasing the robustness to measurement noise

The conventional utilized alternating projection (AP) algorithm for FPM reconstruction is sensitive to measurement noise [10]. This results in the required long exposure time for high SNR measurements and largely limits FPM's practical applications. To deal with low SNR inputs, various FPM reconstruction algorithms have been proposed with stronger robustness to measurement noise.

Based on the Wirtinger derivatives [20–22], Bian et al. [23] utilized the gradient descent scheme to implement FPM reconstruction. An additional noise relaxation constraint is introduced to effectively attenuate Gaussian measurement noise. Following the gradient descent scheme, Yeh et al. [34] tested different objective functions (intensity based, amplitude based, and Poisson maximum-likelihood) for FPM reconstruction. The results show that the amplitude-based and Poisson maximum-likelihood objective functions produce better results than the intensity-based objective function. The conclusion offers an intuitional guide for effective FPM reconstruction.

Besides Gaussian noise, there exist other kinds of noise in the measurements, including Poisson noise and speckle noise, which are common when illumination is spatially and temporally coherent (such as the laser FPM system [28, 30]). To efficiently handle these measurement noise, Bian et al. [35] incorporated the Poisson maximum-likelihood optimization model and the truncated Wirtinger gradient [36] together into a gradient descent framework. The utilized truncated gradient can efficiently distinguish various noise from measurements and prevent them from degrading the reconstruction. Zuo et al. [37] introduced an adaptive step-size strategy to the AP method to deal with measurement noise with less computational complexity. The strategy works because the step size gradually decreases as the iteration proceeds, which effectively improves the stability and robustness of the reconstruction and retains the fast convergence speed of AP.

The above algorithms are non-convex and need careful initialization for convergence to the global optimum. Utilizing the convex semi-definite programming (SDP)-based phase-retrieval scheme [10], Horstmeyer et al. [38] modeled FPM reconstruction as a convex optimization process, by rewriting the quadratic equations in

Eq. (2) as linear equations in a higher dimension [39]. This method guarantees global optimum by a series of convex relaxations, but requires matrix lifting to work in a higher matrix space and, thus, takes a heavy computation load. For example, it takes the algorithm ~130 s to reconstruct a 1-megapixel image with GPU acceleration, while the AP algorithm needs only ~15 s for the same reconstruction.

3.3 Correcting system aberrations

Besides measurement noise, there may exist other system aberrations in an FPM setup, including pupil function aberration, pupil location offset, and sample motion. Pupil function aberration is caused by imperfect lens fabrication, resulting in an non-ideal circular function with globally inconsistent phase. Pupil location offset is caused by LED misalignment. Although one can pre-characterize these aberrations [40], such a procedure can be exhaustive and laborsome because the aberrations are sensitive to the movement of system elements. Sample motion arises due to many reasons. For endoscopy applications, hand-held endoscope probes may move during multiple acquisitions of the sample. In transmission electron microscopy, sample drift is a common problem for multiple image acquisitions. Therefore, multiple computational aberration correction methods have been proposed for effective FPM reconstruction.

Bian et al. [41] used an image-quality metric as a guide star in a global optimization framework and realized adaptive wavefront correction to compensate pupil function aberration. However, this approach takes heavy computation load and can correct only a limited number of low-order aberrations. To compensate high-order aberrations, Ou et al. [18] proposed the embedded pupil function recovery (EPRY) method that reconstructs pupil function simultaneously with HR spatial-frequency spectrum under the AP optimization scheme. Similar to the simultaneous probe retrieval in ptychography [42], this technique allows for the removal of spatially varying aberrations throughout the microscope's wide FOV. However, it is susceptible to system initialization and easily trapped in a local optimum [26]. Zhang et al. [43] proposed to jointly optimize pupil function and HR spatial-frequency spectrum under a gradient-descent scheme, by fitting reconstruction with measurements following a squared-error metric. Benefiting from the joint optimization strategy, the algorithm owns stronger robustness than the EPRY method.

Because each LED position corresponds to an incident angle and, thus, a certain shift of sample's spatial-frequency spectrum in the Fourier domain, LED misalignment would introduce pupil location offset that degrades FPM reconstruction. To deal with this problem, an additional location searching operation using the simulated annealing algorithm is introduced into the reconstruction, to estimate and compensate the offset [34, 44]. This is similar to the technique correcting the probe function shift in conventional ptychography [45]. In addition, the aforementioned truncated Poisson Wirtinger Fourier ptychographic reconstruction method [35] can also tackle this problem because the introduced truncated gradient is able to remove the measurement outliers caused by pupil location offset and produce aberration-free reconstruction.

Sample motion is common in microscopy and would also degrade the FPM reconstruction. To tackle this problem, Bian et al. [46] introduced a simulated annealing module into the adaptive optimization framework [25], to search for the unknown sample shift during each capture. The estimated shift is then utilized to compensate the sub-spectrum's phase offset caused by sample motion. The technique can correct for unknown sample motion with its standard deviation being up to 10% of the FOV. Considering that sample motion would introduce image blur, Ma et al. [47] designed a temporal coded illumination sequence in each single capture and realized linear motion deblurring for moving samples.

4 Extensions of FPM

Conventional FPM replaces a microscope's illumination source with an LED array to provide angularly varying illumination. There are alternative FPM modalities adapted for different imaging scenarios.

Besides angular illumination, aperture scanning is also able to obtain different spatial-frequency sub-spectra of the sample [48–50], as shown in Figure 3A. The aperture scanning scheme circumvents the thin specimen requirement of conventional FPM, because the phase-retrieval reconstruction is now limited to the unchanging 2D wavefront exiting the sample (the light field scattered by the sample's 3D distribution). For conventional FPM, if the sample is too thick, the simple correlation between the change of illumination angle and the spectrum shift in Fourier space is no longer valid due to tissue scattering, which leads to failed reconstruction. The aperture scanning scheme also enables 3D refocusing [49] and super-resolution macroscopic imaging [48, 50]. Benefiting from the low cost and high quality of current cell

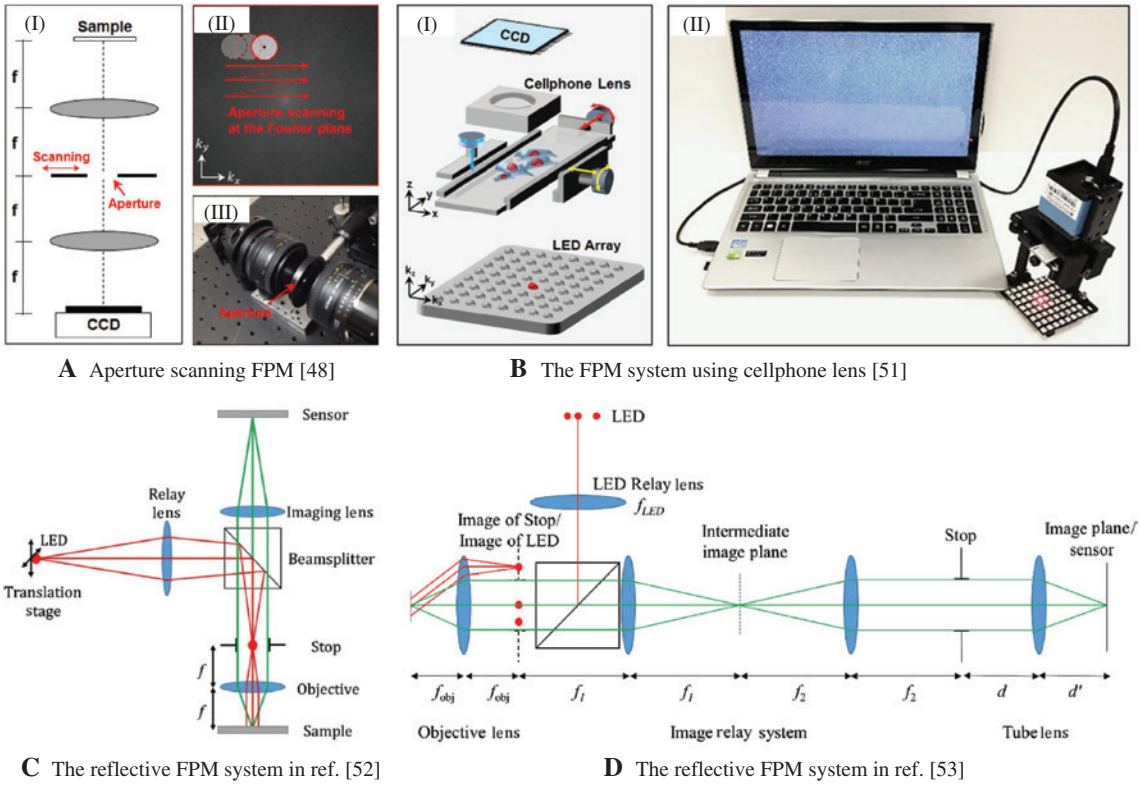

A Aperture scanning FPM [48]

B The FPM system using cellphone lens [51]

C The reflective FPM system in ref. [52]

D The reflective FPM system in ref. [53]

Figure 3: Extended FPM modalities. (A) The aperture scanning FPM system in Ref. [48]. (B) The 3D printed FPM system using a cellphone lens [51] is shown. (C) and (D) The light paths of two reflective FPM systems [52, 53].

phone lens, Dong et al. [51] built a portable FPM setup using a cell phone lens and 3D printed modules instead of a commercial microscope, as shown in Figure 3B. The platform enables healthcare accesses in low-resource settings. Chung [54] incorporated the FPM setup into a fluorescence microscope and utilized the reconstructed pupil function to correct aberrations for wide-FOV high-resolution fluorescence imaging. Different from the above FPM systems in a transmissive mode, Pacheco et al. [52, 53] implemented FPM in a reflective mode, as shown in Figure 3C and D. This configuration offers great potentials in tissue imaging and optical inspection.

The captured low-resolution images are not limited to being stitched together for 2D high-resolution imaging. The information contained in the images can be further explored as follows. (I) The FPM system can be extended for 3D tomographic imaging of a thick sample, by employing either the multislice coherent model [55] or the first Born approximation (diffraction tomography theory) [56]. Using the technique, each captured image is treated as the composition of different sample layers, and the sample's volumetric refractive index reflecting its transparent and contiguous features can be quantitatively reconstructed without the need of interferometry or any moving parts. (II) Tian et al. [57, 58] utilized the FPM system for 3D differential phase contrast (DPC) microscopy, by digitally refocusing the captured images through various depths via light field processing. (III) The FPM system can also be applied for brightfield, darkfield, and phase-contrast imaging by applying different LED-lightening patterns [59, 60]. All the above extensions demonstrate great potentials of FPM for various imaging applications.

5 Conclusions

To conclude, we have revisited the theoretical principles of Fourier ptychographic microscopy. It brings together two innovations in computational optics to bypass the space-bandwidth-product barrier, including the phase-retrieval reconstruction and the aperture synthesis technique. In this way, it is able to acquire both the sample's high-resolution amplitude and phase information computationally, and get rid of hardware design difficulties and enable high compatibility with current microscopes. Therefore, it has been applied to multiple imaging modalities, and shows great potentials for various biological applications in life science.

Funding: National Natural Science Foundation of China, Funder Id: 10.13039/501100001809, Grant no. 61327902.

References

[1] G. Zheng, R. Horstmeyer and C. Yang, Nat. Photonics 7, 739–745 (2013).
[2] A. W. Lohmann, R. G. Dorsch, D. Mendlovic, C. Ferreira and Z. Zalevsky, J. Opt. Soc. Am. A 13, 470–473 (1996).
[3] G. Zheng, X. Ou, R. Horstmeyer, J. Chung and C. Yang, Opt. Photonics News 25, 26–33 (2014).
[4] J. R. Gilbertson, J. Ho, L. Anthony, D. M. Jukic, Y. Yagi, et al., BMC Clin. Pathol. 6, 4 (2006).
[5] X. Ou, R. Horstmeyer, C. Yang and G. Zheng, Opt. Lett. 38, 4845–4848 (2013).
[6] J. Goodman, in 'Introduction to Fourier Optics', (McGraw-Hill, New York, 2008).
[7] R. Horstmeyer and C. Yang, Opt. Express 22, 338–358 (2014).
[8] J. R. Fienup, Appl. Optics 21, 2758–2769 (1982).
[9] J. R. Fienup, J. Opt. Soc. Am. A 4, 118–123 (1987).
[10] Y. Shechtman, Y. C. Eldar, O. Cohen, H. N. Chapman, J. Miao, et al., IEEE Signal Proc. Mag. 32, 87–109 (2015).
[11] X. Ou, R. Horstmeyer, G. Zheng and C. Yang, Opt. Express 23, 3472–3491 (2015).
[12] J. Sun, C. Zuo, L. Zhang and Q. Chen, Sci. Rep. 7, 1187 (2017).
[13] A. Williams, J. Chung, X. Ou, G. Zheng, S. Rawal, et al., J. Biomed. Opt. 19, 066007–066007 (2014).
[14] R. Horstmeyer, X. Ou, G. Zheng, P. Willems and C. Yang, Comput. Med. Imaging Graph. 42, 38–43 (2015).
[15] J. Chung, X. Ou, R. P. Kulkarni and C. Yang, PLoS One 10, e0133489 (2015).
[16] J. Kim, B. M. Henley, C. H. Kim, H. A. Lester and C. Yang, Biomed. Opt. Express 7, 3097–3110 (2016).
[17] S. Dong, R. Shiradkar, P. Nanda and G. Zheng, Biomed. Opt. Express 5, 1757–1767 (2014).
[18] X. Ou, G. Zheng and C. Yang, Opt. Express 22, 4960–4972 (2014).
[19] S. Dong, Z. Bian, R. Shiradkar and G. Zheng, Opt. Express 22, 5455–5464 (2014).
[20] R. Remmert, in 'Theory of Complex Functions', (Springer, New York, 1991).
[21] R. F. H. Fischer, in 'Precoding and Signal Shaping for Digital Transmission', (John Wiley & Sons, New York, 2005).
[22] E. J. Candes, X. Li and M. Soltanolkotabi, IEEE Trans. Inf. Theory 61, 1985–2007 (2015).
[23] L. Bian, J. Suo, G. Zheng, K. Guo, F. Chen, et al., Opt. Express 23, 4856–4866 (2015).
[24] J. Sun, Q. Chen, Y. Zhang and C. Zuo, Opt. Express 24, 15765–15781 (2016).
[25] L. Bian, J. Suo, G. Situ, G. Zheng, F. Chen, et al., Opt. Lett. 39, 739–745 (2014).
[26] K. Guo, S. Dong, P. Nanda and G. Zheng, Opt. Express 23, 6171–6180 (2015).
[27] Z. F. Phillips, M. V. D'Ambrosio, L. Tian, J. J. Rulison, H. S. Patel, et al., PLoS One 10, e0124938 (2015).
[28] J. Chung, H. Lu, X. Ou, H. Zhou and C. Yang, Biomed. Opt. Express 7, 4787–4802 (2016).
[29] Y. Zhang, W. Jiang, L. Tian, L. Waller and Q. Dai, Opt. Express 23, 18471–18486 (2015).
[30] C. Kuang, Y. Ma, R. Zhou, J. Lee, G. Barbastathis, et al., Opt. Express 23, 26999–27010 (2015).
[31] L. Tian, X. Li, K. Ramchandran and L. Waller, Biomed. Opt. Express 5, 2376–2389 (2014).
[32] L. Tian, Z. Liu, L.-H. Yeh, M. Chen, J. Zhong, et al., Optica 2, 904–911 (2015).
[33] Y. Zhou, J. Wu, Z. Bian, J. Suo, G. Zheng, et al., J. Biomed. Opt. 22, 066006–066006 (2017).
[34] L.-H. Yeh, J. Dong, J. Zhong, L. Tian, M. Chen, et al., Opt. Express 23, 33214–33240 (2015).
[35] L. Bian, J. Suo, J. Chung, X. Ou, C. Yang, et al., Sci. Rep. 6, 27384 (2016).
[36] Y. Chen and E. Candes, Adv. Neural Inform. Process. Syst. 70, 739–747 (2015).
[37] C. Zuo, J. Sun and Q. Chen, Opt. Express 24, 20724–20744 (2016).
[38] R. Horstmeyer, R. Y. Chen, X. Ou, B. Ames, J. A. Tropp, et al., New J. Phys. 17, 053044 (2015).
[39] L. Vandenberghe and S. Boyd, SIAM Rev. 38, 49–95 (1996).
[40] G. Zheng, X. Ou, R. Horstmeyer and C. Yang, Opt. Express 21, 15131–15143 (2013).
[41] Z. Bian, S. Dong and G. Zheng, Opt. Express 21, 32400–32410 (2013).
[42] A. M. Maiden and J. M. Rodenburg, Ultramicroscopy 109, 1256–1262 (2009).
[43] Y. Zhang, W. Jiang and Q. Dai, Opt. Express 23, 33822–33835 (2015).
[44] J. Sun, Q. Chen, Y. Zhang and C. Zuo. Biomed. Opt. Express 7, 1336–1350 (2016).
[45] A. M. Maiden, M. J. Humphry, M. C. Sarahan, B. Kraus and J. M. Rodenburg, Ultramicroscopy 120, 64–72 (2012).
[46] L. Bian, G. Zheng, K. Guo, J. Suo, C. Yang, et al., Biomed. Opt. Express 7, 4543–4553 (2016).
[47] C. Ma, Z. Liu, L. Tian, Q. Dai and L. Waller, Opt. Lett. 40, 2281–2284 (2015).
[48] S. Dong, R. Horstmeyer, R. Shiradkar, K. Guo, X. Ou, et al., Opt. Express 22, 13586–13599 (2014).
[49] X. Ou, J. Chung, R. Horstmeyer and C. Yang. Biomed. Opt. Express 7, 3140–3150 (2016).
[50] J. Holloway, M. S. Asif, M. K. Sharma, N. Matsuda, R. Horstmeyer, et al., IEEE Trans. Comput. Imaging 2, 251–265 (2016).
[51] S. Dong, K. Guo, P. Nanda, R. Shiradkar and G. Zheng, Biomed. Opt. Express 5, 3305–3310 (2014).
[52] S. Pacheco, B. Salahieh, T. Milster, J. J. Rodriguez and R. Liang, Opt. Lett. 40, 5343–5346 (2015).
[53] S. Pacheco, G. Zheng and R. Liang, J. Biomed. Opt. 21, 026010–026010 (2016).
[54] J. Chung, J. Kim, X. Ou, R. Horstmeyer and C. Yang. Biomed. Opt. Express 7, 352–368 (2016).
[55] L. Tian and L. Waller. Optica 2, 104–111 (2015).
[56] R. Horstmeyer, J. Chung, X. Ou, G. Zheng and C. Yang, Optica 3, 827–835 (2016).
[57] L. Tian, J. Wang and L. Waller. Opt. Lett. 39, 1326–1329 (2014).
[58] L. Tian and L. Waller. Opt. Express 23, 11394–11403 (2015).
[59] Z. Liu, L. Tian, S. Liu and L. Waller. J. Biomed. Opt. 19, 106002–106002 (2014).
[60] K. Guo, S. Dong and G. Zheng, IEEE J. Select. Topics Quant. 22, 77–88 (2016).